Morpho-Structural and magnetic properties of CoFe2O4/SIO2 nanocomposites: effect of the molecular coating

Sawssen Slimani*[1,3], Alessandro Talone[2,3], Maryam Abdolrahimi[2,3], Patrizia Imperatori[3], Gianni Barucca[3,4], Dino Fiorani[3] and Davide Peddis[1,3].

[1]*Università degli Studi di Genova, Dipartimento di Chimica e Chimica Industriale, Via* Dodecaneso 31, 1-16146 Genova, Italy.
[2]*Dipartimento di Scienze, Università degli Studi 'Roma Tre', Roma, Italy.*
[3]*Istituto di Struttura della Materia-CNR, 00015 Monterotondo Scalo (RM), Italy.*
[4]*Dipartimento di Scienze e Ingegneria della Materia, dell'Ambiente ed Urbanistica-SIMAU, Università Politecnica delle Marche, Ancona, Italy.*

Abstract

The use of magnetic nanoarchitectures in several applications is often limited by the lack of non-interacting particles, due to the frequent presence of clusters and aggregates of particles. Here we report an investigation of the interparticle interactions by changing the molecular coating on ~5 nm $CoFe_2O_4$ nanoparticles embedded in a silica structure. The magnetic investigation at low temperature allows revealing the key role of organic ligands in tuning the morpho-structural properties of hybrid materials. Cobalt ferrite coated nanoparticles were prepared by polyol method using triethylene glycol as co-reagent (CFO_T), and by exchange ligand process using dihydroxyhydrocinnamic acid (CFO_H). Then, magnetic mesoporous silica nanocomposites have been prepared starting from CFO_T (CFO_{TS}) and CFO_H (CFO_{HS}). For CFO_{TS} sample the interparticle distance did not change after coating, whereas CFO_{HS} sample showed an increase in the interparticle distance by 23%. This value has been obtained investigating interparticle interactions by remanence techniques, which represent a good approach to determine approximated values of interparticle distances in complex systems. The measurements showed that the silica coating produces 47% reduction in the dipolar interaction strength for CFO_{HS} sample, whereas no significant change was observed for the CFO_{TS} sample. The differences in magnetic response upon varying the molecular coating of nanoparticles are due to the different interactions of the molecular ligands with the silica, resulting in a change of interparticle distances and then magnetic interactions.

* Corresponding author: Sawssen.Slimani@edu.unige.it

1. Introduction

Due to their unique size and shape dependent properties, single domain magnetic nanoparticles (MNPs) have been the subject of extensive investigations of their fundamental properties which opened the way to a variety of applications, such us in biomedicine (biological entities separation[1–3], drug delivery[4,5], hyperthermia for cancer therapy[6–8] and magnetic resonance imaging (MRI[9–11])).

Magnetic nanoparticles-based hybrid materials (MNP-HM) represent promising multifunctional systems with novel magnetic properties, due to interface effects, and superior performance in technological applications[12,13].

In this framework, the design of suitable synthetic approach represents a key point to obtain a MNP-HM with optimized physical properties. A key step in the synthesis of MNP-HM is definitively the molecular functionalization of magnetic nanoparticles. To date, various strategies have been exploited, such as creating magnetic core-shell structures[14], using polymeric protective ligands to bond with nanoparticle surface[15], creating an electrostatic layer on the particle surface in order to avoid aggregations. The substitution of the native surface ligands with aromatic molecule ligands also has been widely studied [16–18]. While the existing literature provides numerous options for many derivatives of these systems, there are few examples of the use of dihydroxyhydrocinnamic acid (i.e., dihydrocaffeic acid) ligand (HCA)[19–21].

Here, we report a synthetic strategy that allows to prepare weakly interacting nanoparticles and a detailed investigation of their morpho-structural and magnetic properties. On the other hand, various biomolecules have been immobilized on mesostructured silica (MS)[22] which is used as a matrix for a variety of extraction, purification, recovery[23], and delivery systems[24] due to its high surface area, a large pore volume and regular pore size distributions. MNPs must be also functionalized to make them biocompatible for biomedical or environmental applications. MNPs are often covered by non-magnetic inorganic materials such as zirconia[25], titania[26], or silica[27,28]. Given its known biocompatibility, as well as its relative ease of synthesis, silica has always been widely used as a coating shell in several applications. In this contest, mesoporous silica-based nanocomposites have been the suitable candidates materials for most of the applications not only for their interesting textural properties but also for the possibility to manipulate them by simply applying an external magnetic field due to presence of MNPs as one of their components.

Using as a case study the $CoFe_2O_4/SiO_2$ hybrid material, this paper focus on the investigation of the role of MNPs' molecular coating in the formation of magnetic nanocomposites. In detail, ~5 nm cobalt ferrite nanoparticles have been prepared by polyol method, using triethylene glycol (TEG) as co-reagent, CFO_T. Then, TEG adsorbed on particle's surface has been replaced by exchange ligand process with dihydrocaffeic acid (HCA), CFO_H. Then, magnetic mesoporous silica nanocomposites have been prepared starting from CFO_T (CFO_{TS}) and CFO_H (CFO_{HS}), investigating the evolution of morpho-structural and most of all the magnetic properties of the materials.

2. Experimental Section

2.1 Materials and chemicals

Iron (III) nitrate nonahydrate (Fe $(NO_3)_3 \cdot 9H_2O$) (≥98%, Sigma -Aldrich), cobalt (II) nitrate hexahydrate ($Co(NO_3)_2.6H_2O$)(≥98%, Sigma Aldrich), Triethylene glycol (TEG)(≥99%, Sigma-Aldrich), Tetraethyl orthosilicate (TEOS) (≥99%, Sigma-Aldrich), (CTAB) (≥99%,Sigma-Aldrich),Tetrahydrofuran(THF) (≥99%,Sigma-Aldrich), 3,4 Dihydroxyhydrocinnamic acid (HCA) (≥98%, Sigma Aldrich), Sodium hydroxide (NaOH) (Sigma-Aldrich) were used. All chemicals were reagent grade and used without further purification or modification.

2.2 Synthesis of magnetic nanoparticles

Cobalt ferrite magnetic nanoparticles CFO were synthesized using polyol chemical method with some modifications[29–31]. In brief, 2 mmol of Fe $(NO_3)_3 \cdot 9H_2O$ and 1 mmol of Co $(NO_3)_2.6H_2O$ were dissolved in 1 ml of distilled water. The mixture was added to 100 ml of TEG under magnetic stirring and heated to the boiling point of the solvent using a mantle. Once the boiling point is attended, the solution was kept under reflux for 2 hours. After the solution was cooled to room temperature, the nanoparticles were washed with acetone and collected by centrifugation (10 min, 6000 rpm). The removal procedure was repeated three times and the nanoparticles were dried in the oven at 60°C overnight. The sample is named CFO_T.

2.3 Ligand exchange procedure

Detailed description of the HCA exchange ligand procedure has been reported elsewhere[32]. Briefly, 38 mg of MNPs has been sonicated in 3 ml of Tetrahydrofuran (THF) for 30 minutes. 38 mg of HCA were dissolved in 7,5 ml of THF. Then the solution of HCA was added to the MNPs, and the mixture was magnetically stirred for 3 hours at 50°C in a water bath. Afterward, 3 ml of 0.5 M NaOH was added to precipitate the product. The precipitate was washed 3 times with THF and redispersed in water. The obtained exchanged nanoparticles sample was labeled as CFO_H.

2.4 Mesoporous silica coating

Mesoporous silica coated MNPs was prepared following sol-gel method based on the hydrolysis and poly-condensation of Tetraethyl orthosilicate (TEOS) in a basic environment[33]. Briefly, 50 mg of CFO_T nanoparticles was added to 250 mg of hexadecyltrimethylammonium bromide (CTAB) dissolved and sonicated for 30 min in 20 ml of water, followed by the addition of 100 ml of 2M NaOH solution under stirring. The solution was heated at 80 °C. Then, 1.25 µl of TEOS were added dropwise. The solution was kept at 80 °C under vigorous stirring for 2h. The obtained nanoparticles were washed and collected by filtration and dried at 60°C overnight. The obtained sample was named CFO_{TS}. To synthesize CFO_{HS} nanocomposite, the same previous coating procedure was repeated starting from magnetic nanoparticles coated with HCA (CFO_H).

2.5 Experimental techniques

X-ray diffraction (XRD) was carried out using Seifert 3003 TT diffractometer equipped with a secondary graphite monochromator, using CuKα radiation (λ = 1.5418 Å). The measurements were performed in the 2θ range 20-80° with a step size of 0.04°, counting 4s per step.

Transmission electron microscopy (TEM) observations were performed by means a Philips CM200 microscope operating at 200 kV and equipped with LaB6 filament. For analysis, samples were prepared in form of suspension putting the MNPs or the magnetic nanocomposites in ethanol (1mg/mL). A drop of the suspension was deposited on a carbon coated TEM grid kept in air until complete solvent evaporation.

Transmittance intensity versus wavenumber in the range of 400 cm^{-1}- 4000 cm^{-1} for all the samples analysis were acquired on Fourier-transform infrared spectroscopy (FT-IR) with a Shimadzu IR Prestige-21, equipped with a Specac Golden Gate Single Reflection Diamond Attenuated total reflection (ATR).

Superconducting quantum interference device (SQUID) Quantum Design magnetometer was used to study the magnetic properties of all the samples. Samples in form of powder was fixed in a polycarbonate capsule using epoxy resin to prevent the movement of the particles during the measurements. Field-dependent magnetization measurements were performed at 5K, and the thermal dependence of magnetization was measured according to zero field cooled (ZFC) and field cooled (FC) protocols. In ZFC magnetization measurements first the sample is cooled in zero magnetic field, then the magnetization is measured during warming up the sample in a small applied field (2.5 mT). The FC magnetization process starts maintaining the applied field and measuring the magnetization during cooling down the sample.

Field dependence of remanent magnetization was investigated by IRM (Isothermal Remanent Magnetization) and DCD (Direct Current Demagnetization) protocols. The IRM protocol starts from a sample in a demagnetized state. First a small positive magnetic field is applied (H_{rev}), then the field is removed and the remanence M_{IRM} is measured (i.e., in zero field). This experimental process is repeated by increasing the applied field until the remanence takes the saturation value. In DCD measurement, we start from a saturated sample, then a small field in the opposite direction of magnetization is applied for few seconds, then the field is switched off and the remanence M_{DCD} is measured. The process is repeated increasing the magnetic field until the remanence reaches the saturation value.

3. Results and Discussion

Spinel structure of cobalt ferrite nanoparticles was confirmed by X-ray power diffraction measurements (XRD, Figure S1a, pdf card JCPDS 3-864) [34]. The Crystallite size was estimated from Scherrer equation to be about 5.7(2) nm (supporting information).

To investigate the interactions between molecules and nanoparticles, FT-IR spectroscopy was performed on all samples as well as on TEG and HCA (Figure 1). FT-IR Spectrum of CFO_T sample (Figure 1a) shows the characteristic absorption of TEG, (i.e., the stretching vibration of O-H molecules around 3400 cm^{-1}, the symmetric and asymmetric stretching vibrations of -CH_2

groups identified in the region of 2750 to 3000 cm^{-1} [,35] and the stretching vibration of C-O bond observed in the range of 1060 cm^{-1} to 1130 cm^{-1} [, 36]) together with the signal due to the metal-oxygen (M-O) stretching vibration at 565 cm^{-1} [37]. The CFO_{TS} spectrum(Figure 1a) beyond the absorption due to the M-O stretching mode at 567 cm^{-1} clearly shows the presence of silica: the peaks at 1085 cm^{-1} and 810 cm^{-1} are ascribed to the asymmetric and symmetric Si-O-Si stretching vibrations respectively[38], the bond at 954 cm^{-1} belongs to Si-OH silanol group. For CFO_{TS} spectrum, the characteristic peaks of TEG were not clearly visible, suggesting the strong interactions between TEG molecules and the silica that leads to weakened vibrations modes of the TEG molecules[39]. Figure 1b shows the FT-IR spectra of CFO_T covered by exchange ligand process with HCA, CFO_H and silica coated CFO_H (CFO_{HS}) nanocomposite. A shift of the characteristic bonds of HCA (bonds observed at 1620 cm^{-1} and at 1524 ,1450 cm^{-1} assigned to the presence of aromatic ring C=C stretching vibration[40] and the C–C skeletal vibration of aromatic ring[40,41] respectively and the absorption at 1200 cm^{-1} ascribed to the phenolic O-H deformation[41]) to 1580 cm^{-1} and 1465, 1340 cm^{-1} is observed in the spectrum of CFO_H sample, confirming the interaction between the HCA ligand and the CFO nanoparticles surfaces. The bond attributed to the vibrations of the crystalline lattice of cobalt ferrite nanoparticles is shadowed in the spectrum of CFO_HCA sample, which is probably due to high ligand concentration[42]. The FT-IR spectrum of CFO_{HS} shows the characteristic peaks of the silica structure. In this case, the M-O stretching vibration was clearly visible in the spectrum of CFO_{HS}, which can be due to the extra washing and drying process performed after the silica coating that removes all the excess of the surfactants and free molecules.

High resolution (HR) TEM analysis of the CFO_T sample shows that it is composed of aggregates of small nanoparticles (Figure 2a). Atomic planes are clearly visible in some particles, correctly oriented with respect to the electron beam, suggesting that they are well crystallized. Good crystallization of the sample is confirmed by selected area electron diffraction (SAED) measurements in which well-defined diffraction rings are visible (Figure S1b). From HR-TEM observations, particles reveal a faceted spherical shape with a mean diameter of around 6 nm, in agreement with XRD measurement. After ligand exchange with HCA (Figure 2b), no change in single particle size or shape was observed, indicating the success of the ligand exchange process used. To investigate the role of MNPs' molecular coating on the properties of nanocomposites, TEM measurements were performed after silica coating of both CFO_T (CFO_{TS}) and CFO_H (CFO_{HS}) samples. Figure 2c shows a typical TEM bright field image of the CFO_{TS} nanocomposite. Large agglomerates of nanoparticles are clearly visible within the silica because of their darker contrast with respect to the matrix. On the other hand, CFO_{HS} sample shows less aggregated particles within the silica structures. In particular, in Figure 2d it is possible to observe the presence of smaller agglomerates of magnetic nanoparticles inside the silica matrix, with a clearer contrast than that visible in Figure 2c characteristic of a lower particles' density. Furthermore, it is possible to notice a sort of parallel stripes inside the silica (inset Figure 2d). This contrast is due to the presence of pores inside the matrix having the shape of long tunnels, which line up in a parallel way giving rise to an ordered texture. A possible explanation for the observed difference on morpho-textured features of the samples

can be ascribed to the reaction of silanes with the polyol (CFO_T) during the synthesis of mesoporous silica based-materials. In detail, during the silica formation process, triethylene glycol (TEG) can react with the silanol groups, forming a hybrid matrix, in which the organic chain is bounded with the Si atom through Si–O–C covalent bonds [39,43–46], affecting the formation of the mesoporous silica structure and the particle aggregations. In case of CFO_{HS} nanocomposite, the presence of HCA ligand dose not contribute to the mesoporous silica formation, and it acts as a protective layer to prevent more nanoparticle aggregations.

3.1 Magnetic properties

Temperature dependence of magnetization was investigated by zero field cooled (ZFC) and field cooled (FC) protocols (Figure 3). In the ideal case, for a sample of non-interacting nanoparticles with identical size, the maximum in ZFC curve corresponds to the blocking temperature, T_b. However, the inevitable size distribution in real systems leads to a broadening of the curve and to a shift of the peak temperature , $T_{max} = \beta T_b$,where β is a coefficient which depends on the type of particle size distribution (β=1.5; 2)[47]. T_b is defined as the temperature at which the relaxation time is equal to the timescale of the experimental technique[48]. In a real system of nanoparticles, T_b is often defined as the temperature at which 50% of the particles are in superparamagnetic regime[49,50]. Since T_b is proportional to the anisotropy energy barrier ($E_a = KV$), an estimate of the T_b distribution can be obtained from the E_a distribution by evaluating the temperature at which 50% of the particles overcome their anisotropy energy barriers[51,52] (Figure S2). An irreversible magnetic behaviour was observed below a given temperature called T_{irr}, which corresponds to the blocking temperature of the particles with higher E_a in the sample[53]. Above T_{irr}, ZFC and FC curves coincide, indicating the presence of all MNPs in a superparamagnetic regime. In presence of interparticle interactions, it has to be considered that they also contribute to the effective anisotropy of the system and then T_{max} depends also on them.

In all the samples, FC magnetization increases as the temperature decreases down to a temperature below which M_{FC} tends to a temperature-independent behaviour, revealing the presence of interparticle interactions, leading to a frozen magnetic ordered state with high anisotropy[54].

The CFO_T and CFO_{TS} samples show very similar values of T_{max} and T_b within the experimental error, suggesting that the silica coating does not influence the magnetization dynamics of the nanoparticles. On the other hand, comparing the CFO_H and CFO_{HS} samples, a decrease in the values of T_{max} and T_b (Table1) in CFO_{HS} is observed suggesting a reduction of the effective anisotropy energy, to which interparticle interactions contribute, when the particles are embedded in a silica structure.[55,56] Moreover, comparing COF_T and COF_H , a lower T_{irr} value is observed for the second one, confirming that surface coating with the HCA exchange ligand produces a reduction of the particles aggregation.[45]

The field dependence of magnetization was investigated at 5 K (Figure 4). The values of saturation magnetization (M_s), coercive field ($\mu_0 H_c$), reduced remanent magnetization (M_r/M_s) and

saturation field ($\mu_0 H_k$) (i.e., the field where the difference between the magnetizing and demagnetizing branches normalized to the M_S value, becomes ≈ 1%)[57], extracted from the hysteresis loops are reported in Table 2. The M_s values for the samples are, within the experimental error, quite close to that of bulk one (83−90 Am^2kg^{-1}). However, coercivity, saturation field and reduced remanent magnetization (M_r/M_s) show a quite complex behaviour. A lower M_r/M_s value was observed in CFO_{HS} (∼0.62) sample with respect to that of CFO_H (∼0.7) sample.

Previous studies have investigated the interaction of polyols with TEOS, establishing the influence of these additives on silica structures formation[34–37]. This means that during the synthesis of CFO_{TS} nanocomposite , the TEG molecules present on nanoparticles surface can chemically interacts with the silanol groups: the organic chain is bounded with the Si atom through Si–O–C covalent bonds [30,] . Consequently, it results more aggregates of particles inside silica matrix. This could explain the increases of M_r/M_s suggesting an increase of interparticle interactions. On the other hand, using HCA as a coating ligand instead of TEG, leads to a dispersion of nanoparticles inside ordered silica structure. CFO_{HS} nanocomposite shows a decrease in the M_r/M_s value indicating a reduction in the interparticle interactions among particles [58]. Moreover, the reduction of coercivity indicates that the system becomes less anisotropic. Similar results have reported that M_r/M_s increases with increasing particle interactions[59]. However others find that the reduced remanence decreases with increasing the interactions[60–62]. Monte Carlo simulations reported by Kechrakos et al. suggest that reduced remanence can increase or decrease depending upon the interparticle interactions strength[63].

The lowest coercive field value is observed for CFO_{HS}, as an effect of the reduction of surface anisotropy due to the HCA ligand. Such effect is combined with that of the silica matrix. This confirms the role of ordered silica structure that leads to a distribution of the particles along the channels minimizing the dipolar interactions in the sample[58].

The empty symbols in Figure 4 represent the low temperature (5 K) direct current demagnetization (DCD) remanent curves. Generally, only the blocked particles contribute to the remanent magnetization. The obtained M_{DCD} is only sensitive to the irreversible component of the magnetization and the value of the field at which the remanent magnetization is equal to zero, called remanence coercivity, H_{Cr} corresponds to the mean switching field. The decrease in the H_c , H_k and H_{cr} values for CFO_{HS} nanocomposite , also was an indication that the ligand exchange with HCA induces a decrease of the magnetic anisotropy .On the other hand, for CFO_{TS} nanocomposite the ordered silica structure was not obtained as seen from TEM images, which support the possible interaction between TEG polyol and TEOS during the silica phase formation.

3.2 Investigating nanoparticles arrangement by interparticle interactions.

The investigation of interparticle interactions allows us to get information about nanoparticles arrangement in the different systems.

For an ensemble of nanoparticles with average magnetic moment μ and average separation d, the interaction energy, due to the dipole – dipole interaction, can be expressed by [64]:

$$E_d \approx \frac{\mu_0 \mu^2}{4\pi d^3} \qquad (1)$$

The effect of interparticle interactions has been investigated by means of DCD and IRM measurements carried out at 5K (supporting information) [65]. For non-interacting single-domain particles with uniaxial anisotropy and magnetization reversal by coherent rotation, the IRM and DCD curves are related via the equation[65]:

$$\Delta M = m_{DCD}(H) - 1 + 2m_{IRM}(H) \qquad (2)$$

where $m_{DCD}(H)$ and $m_{IRM}(H)$ represent the reduced terms $M_{DCD}(H)/M_{DCD}(H_{max})$ and $M_{IRM}(H)/M_{IRM}(H_{max})$, with $M_{DCD}(H_{max})$ and $M_{IRM}(H_{max})$ being the remanence values for the DCD and IRM curves for a large reversal field H_{max} capable of fully saturate the sample. The negative ΔM deviation, shown in Figure 5 indicates the prevalence of dipolar interparticle interactions for all the samples. It's worth mentioning that the application of ΔM approach to particles with cubic anisotropy should give positive deviation[66,67]. For CFO_{TS} sample, the dipolar interaction strength does not change with the silica coating (Figure 5a), whereas for CFO_{HS} sample the presence of silica coating produces 47% reduction in the ΔM strength compared to that of CFO_H sample (Figure 5b). The study of magnetic interactions among nanoparticles can be further improved calculating, as a first approximation, a mean value of interactions field(H_{int})[68,69] between the particles:

$$H_{int} = \frac{H'_r - H_r}{2} \qquad (3)$$

where H'_r and H_r correspond to the position of the maxima of the field derivative of the $m_{DCD}(H)$ and $m_{IRM}(H)$ curves, i.e., the maximum of the irreversible susceptibility (Figure S3), which maps the switching field distribution. [70,71] The values of H_{int} were -10 mT and -12 mT for CFO_{HS} and CFO_{TS}, respectively, indicating higher interparticle interactions in the latter one. Considering the dominance of the dipolar interactions and the fact that the magnetic nanoparticles are coming from the same synthesis batch, the difference in the strength of interactions between CFO_{HS} and CFO_{TS} samples can be discussed on the basis of the change of interparticle distance.

Assuming a point dipole model for a sample of randomly distributed nanoparticles, where the maximum distance is considered from the center to the center, an approximation of the interparticle distance d, can be given by:

$$\frac{d_{coated}}{d_{Bare}} \approx \sqrt[3]{\frac{E_{d\ Bare}}{E_{d\ Coated}}} \sim \sqrt[3]{\frac{\Delta M_{Bare}}{\Delta M_{Coated}}} \qquad (4)$$

CFO_{HS} sample shows an interparticle distance (~1.23) higher than that of CFO_{TS} (~0.98) sample (Figure 6), indicating weaker interparticle interactions in CFO_{HS} sample.

4. Conclusions

We have investigated, the effect of MNPs' molecular coating in the formation of ~5 nm $CoFe_2O_4$-based magnetic nanocomposites. The thorough magnetic characterization of all the samples

shows that for CFO_{HS} nanocomposite the coating produces a decrease in the strength of interparticle interactions, corresponding to a reduction of 47%, as shown by ΔM plots, which allow an estimation of the interparticle interaction in complex systems. This finding is consistent with a better dispersion of nanoparticles within the ordered silica matrix and a decrease of interparticle distance, providing evidence that the choice of a suitable molecular coating allows to get a system with small interparticle interactions. Magnetic investigation at low temperature allows verifying such approach used in tuning the strength of interparticle interactions, which is of paramount importance for applications, as they require homogeneous and non-interacting nanoparticles systems.

ACKNOWLEDGMENTS

The authors acknowledge the support from the Horizon Europe EIC Pathfinder Open Program: under grant agreement No. 101046909 (REMAP) and from Project code PE0000021, Concession Decree No. 1561 of 11.10.2022 adopted by "Ministero dell' Universita` e della Ricerca (MUR", according to attachment E of Decree No. 1561/2022, Project title "Network 4 Energy Sustainable Transition-NEST."

References

(1) Yu, C. H.; Tam, K. Y.; Lo, C. C. H.; Tsang, S. C. Species for Magnetic Separation. *October* **2007**, *43* (6), 2436–2438.

(2) Ma, Y.; Chen, T.; Iqbal, M. Z.; Yang, F.; Hampp, N.; Wu, A.; Luo, L. Applications of Magnetic Materials Separation in Biological Nanomedicine. *Electrophoresis* **2019**, *40* (16), 2011–2028. https://doi.org/10.1002/elps.201800401.

(3) Eivazzadeh-Keihan, R.; Bahreinizad, H.; Amiri, Z.; Aliabadi, H. A. M.; Salimi-Bani, M.; Nakisa, A.; Davoodi, F.; Tahmasebi, B.; Ahmadpour, F.; Radinekiyan, F.; Maleki, A.; Hamblin, M. R.; Mahdavi, M.; Madanchi, H. Functionalized Magnetic Nanoparticles for the Separation and Purification of Proteins and Peptides. *TrAC - Trends Anal. Chem.* **2021**, *141*, 116291. https://doi.org/10.1016/j.trac.2021.116291.

(4) Kuznetsova, O. V.; Timerbaev, A. R. Magnetic Nanoparticles for Highly Robust, Facile and Efficient Loading of Metal-Based Drugs. *J. Inorg. Biochem.* **2022**, *227* (December 2021), 111685. https://doi.org/10.1016/j.jinorgbio.2021.111685.

(5) Mohammadi Ziarani, G.; Malmir, M.; Lashgari, N.; Badiei, A. The Role of Hollow Magnetic Nanoparticles in Drug Delivery. *RSC Adv.* **2019**, *9* (43), 25094–25106. https://doi.org/10.1039/c9ra01589b.

(6) Narayanaswamy, V.; Al-omari, I. A.; Kamzin, A. S.; Issa, B.; Obaidat, I. M. Tailoring Interfacial Exchange Anisotropy in Hard – Soft Core-Shell Ferrite Nanoparticles for Magnetic Hyperthermia Applications. **2022**.

(7) Pazouki, N.; Irani, S.; Olov, N.; Atyabi, S. M.; Bagheri-Khoulenjani, S. Fe3O4 Nanoparticles Coated with Carboxymethyl Chitosan Containing Curcumin in Combination with Hyperthermia Induced Apoptosis in Breast Cancer Cells. *Prog. Biomater.* **2022**, No. 0123456789. https://doi.org/10.1007/s40204-021-00178-z.

(8) Production, H. R. O. S.; Cervantes, O.; Lopez, R.; Casillas, N.; Knauth, P.; Checa, N.; Cholico, F. A.; Hernandez-guti, R.; Quintero, L. H.; Paz, J. A.; Cano, M. E. A Ferrofluid with Surface Modified Nanoparticles for Magnetic Hyperthermia and High ROS Production. **2022**.

(9) Cheong, S.; Ferguson, P.; Feindel, K. W.; Hermans, I. F.; Callaghan, P. T.; Meyer, C.; Slocombe, A.; Su, C.-H.; Cheng, F.-Y.; Yeh, C.-S.; Ingham, B.; Toney, M. F.; Tilley, R. D. Simple Synthesis and Functionalization of Iron Nanoparticles for Magnetic Resonance Imaging. *Angew. Chemie* **2011**, *123* (18), 4292–4295. https://doi.org/10.1002/ange.201100562.

(10) Salehipour, M.; Rezaei, S.; Mosafer, J.; Pakdin-Parizi, Z.; Motaharian, A.; Mogharabi-Manzari, M. Recent Advances in Polymer-Coated Iron Oxide Nanoparticles as Magnetic Resonance Imaging Contrast Agents. *J. Nanoparticle Res.* **2021**, *23* (2). https://doi.org/10.1007/s11051-021-05156-x.

(11) Dash, A.; Blasiak, B.; Tomanek, B.; Banerjee, A.; Trudel, S.; Latta, P.; Van Veggel, F. C. J. M. Colloidally Stable Monodisperse Fe Nanoparticles as T2Contrast Agents for High-Field Clinical and Preclinical Magnetic Resonance Imaging. *ACS Appl. Nano Mater.* **2021**, *4* (2), 1235–1242. https://doi.org/10.1021/acsanm.0c02848.

(12) Piñeiro, Y.; Gómez, M. G.; Alves, L. de C.; Prieto, A. A.; Acevedo, P. G.; Gudiña, R. S.; Puig, J.; Teijeiro, C.; Vilar, S. Y.; Rivas, J. Hybrid Nanostructured Magnetite Nanoparticles: From Bio-Detection and Theragnostics to Regenerative Medicine. *Magnetochemistry* **2020**, *6* (1), 1–27. https://doi.org/10.3390/magnetochemistry6010004.

(13) Yang, Y.; Jiao, P. Nanomaterials and Nanotechnology for Biomedical Soft Robots. *Mater. Today Adv.* **2023**, *17*, 100338. https://doi.org/10.1016/j.mtadv.2022.100338.

(14) Asgari, M.; Soleymani, M.; Miri, T.; Barati, A. A Robust Method for Fabrication of Monodisperse Magnetic Mesoporous Silica Nanoparticles with Core-Shell Structure as Anticancer Drug Carriers. *J. Mol. Liq.* **2019**, *292*, 111367. https://doi.org/10.1016/j.molliq.2019.111367.

(15) Rezayan, A. H.; Mosavi, M.; Kheirjou, S.; Amoabediny, G.; Ardestani, M. S.; Mohammadnejad, J. Monodisperse Magnetite (Fe3O4) Nanoparticles Modified with Water Soluble Polymers for the Diagnosis of Breast Cancer by MRI Method. *J. Magn. Magn. Mater.* **2016**, *420*, 210–217. https://doi.org/10.1016/j.jmmm.2016.07.003.

(16) Benbenishty-Shamir, H.; Gilert, R.; Gotman, I.; Gutmanas, E. Y.; Sukenik, C. N. Phosphonate-Anchored Monolayers for Antibody Binding to Magnetic Nanoparticles. *Langmuir* **2011**, *27* (19), 12082–12089. https://doi.org/10.1021/la202190x.

(17) Shah, S. T.; Yehye, W. A.; Saad, O.; Simarani, K.; Chowdhury, Z. Z.; Alhadi, A. A.; Al-Ani, L. A. Surface Functionalization of Iron Oxide Nanoparticles with Gallic Acid as Potential Antioxidant and Antimicrobial Agents. *Nanomaterials* **2017**, *7* (10). https://doi.org/10.3390/nano7100306.

(18) Ghosh, S.; Fang, T. H.; Uddin, M. S.; Hidajat, K. Enantioselective Separation of Chiral Aromatic Amino Acids with Surface Functionalized Magnetic Nanoparticles. *Colloids Surfaces B Biointerfaces* **2013**, *105*, 267–277. https://doi.org/10.1016/j.colsurfb.2012.12.037.

(19) Lee, J.; Kim, K. S.; Na, K. Caffeic Acid-Coated Multifunctional Magnetic Nanoparticles for the Treatment and Bimodal Imaging of Tumours. *J. Photochem. Photobiol. B Biol.* **2016**, *160*, 210–216. https://doi.org/10.1016/j.jphotobiol.2016.03.058.

(20) Togashi, T.; Takami, S.; Kawakami, K.; Yamamoto, H.; Naka, T.; Sato, K.; Abe, K.; Adschiri, T. Continuous Hydrothermal Synthesis of 3,4-Dihydroxyhydrocinnamic Acid-Modified Magnetite Nanoparticles with Stealth-Functionality against Immunological Response. *J. Mater. Chem.* **2012**, *22* (18), 9041–9045. https://doi.org/10.1039/c2jm30325f.

(21) Hachani, R.; Birchall, M. A.; Lowdell, M. W.; Kasparis, G.; Tung, L. D.; Manshian, B. B.; Soenen, S. J.; Gsell, W.; Himmelreich, U.; Gharagouzloo, C. A.; Sridhar, S.; Thanh, N. T. K. Assessing Cell-Nanoparticle Interactions by High Content Imaging of Biocompatible Iron Oxide Nanoparticles as Potential Contrast Agents for Magnetic Resonance Imaging. *Sci. Rep.* **2017**, *7* (1), 1–14. https://doi.org/10.1038/s41598-017-08092-w.

(22) Knežević, N. Ž.; Durand, J.-O. Targeted Treatment of Cancer with Nanotherapeutics Based on Mesoporous Silica Nanoparticles. *Chempluschem* **2015**, *80* (1), 26–36. https://doi.org/10.1002/cplu.201402369.

(23) Song, B. Y.; Eom, Y.; Lee, T. G. Removal and Recovery of Mercury from Aqueous Solution Using Magnetic Silica Nanocomposites. *Appl. Surf. Sci.* **2011**, *257* (10), 4754–4759. https://doi.org/10.1016/j.apsusc.2010.12.156.

(24) Wang, Y.; Zhao, Q.; Han, N.; Bai, L.; Li, J.; Liu, J.; Che, E.; Hu, L.; Zhang, Q.; Jiang, T.; Wang, S. Mesoporous Silica Nanoparticles in Drug Delivery and Biomedical Applications. *Nanomedicine Nanotechnology, Biol. Med.* **2015**, *11* (2), 313–327. https://doi.org/10.1016/j.nano.2014.09.014.

(25) Sponchia, G.; Ambrosi, E.; Rizzolio, F.; Hadla, M.; Tedesco, A. Del; Spena, C. R.; Toffoli, G.; Riello, P.; Benedetti, A. Biocompatible Tailored Zirconia Mesoporous Nanoparticles with High Surface Area for Theranostic Applications. *J. Mater. Chem. B* **2015**, *3* (36), 7300–7306. https://doi.org/10.1039/c5tb01424g.

(26) Kiliç, B.; Gedik, N.; Mucur, S. P.; Hergul, A. S.; Gür, E. Band Gap Engineering and Modifying Surface of TiO2 Nanostructures by Fe2O3 for Enhanced-Performance of Dye Sensitized Solar Cell. *Mater. Sci. Semicond. Process.* **2015**, *31* (1), 363–371. https://doi.org/10.1016/j.mssp.2014.12.020.

(27) C. Cannas, A. Musinu, D. Peddis, and G. P.; Dipartimento. Synthesis and Characterization of CoFe2O4 Nanoparticles Dispersed in a Silica Matrix by a Sol-Gel Autocombustion Method. *J. Chem. Mater* **2006**, *18* (16), 3835–3842. https://doi.org/https://doi.org/10.1021/cm060650n.

(28) Torres-Rodríguez, J.; Soto, G.; López Medina, J.; Portillo-López, A.; Hernández-López, E. L.; Vargas Viveros, E.; Elizalde Galindo, J. T.; Tiznado, H.; Flores, D. L.; Muñoz-Muñoz, F. Cobalt–Zinc Ferrite and Magnetite SiO2 Nanocomposite Powder for Magnetic Extraction of DNA. *J. Sol-Gel Sci. Technol.* **2019**, *91* (1), 33–43. https://doi.org/10.1007/s10971-019-05017-z.

(29) Fiévet, F.; Ammar-Merah, S.; Brayner, R.; Chau, F.; Giraud, M.; Mammeri, F.; Peron, J.; Piquemal, J.-Y.; Sicard, L.; Viau, G. The Polyol Process: A Unique Method for Easy Access to Metal Nanoparticles with Tailored Sizes, Shapes and Compositions. *Chem. Soc. Rev.* **2018**, *47* (14), 5187–5233. https://doi.org/10.1039/C7CS00777A.

(30) Feldmann, C. Polyol-Mediated Synthesis of Nanoscale Functional Materials. *Solid State Sci.* **2005**. https://doi.org/10.1016/j.solidstatesciences.2005.01.018.

(31) Joseyphus, R. J.; Matsumoto, T.; Takahashi, H.; Kodama, D.; Tohji, K.; Jeyadevan, B. Designed Synthesis of Cobalt and Its Alloys by Polyol Process. *J. Solid State Chem.* **2007**. https://doi.org/10.1016/j.jssc.2007.07.024.

(32) Kostevšek, N.; Hudoklin, S.; Kreft, M. E.; Serša, I.; Sepe, A.; Jagličić, Z.; Vidmar, J.; Ščančar, J.; Šturm, S.; Kobe, S.; Žužek Rožman, K. Magnetic Interactions and: In Vitro Study of Biocompatible Hydrocaffeic Acid-Stabilized Fe-Pt Clusters as MRI Contrast Agents. *RSC Adv.* **2018**, *8* (26), 14694–14704. https://doi.org/10.1039/c8ra00047f.

(33) Knezevic, N. Z.; Mauriello Jimenez, C.; Albino, M.; Vukadinovic, A.; Mrakovic, A.; Illes, E.; Janackovic, D.; Durand, J.-O.; Sangregorio, C.; Peddis, D. Synthesis and Characterization of Core-Shell Magnetic Mesoporous Silica and Organosilica Nanostructures. *MRS Adv.* **2017**, *2* (19–20), 1037–1045. https://doi.org/10.1557/adv.2017.69.

(34) Yin, N. Q.; Wu, P.; Yang, T. H.; Wang, M. Preparation and Study of a Mesoporous Silica-Coated Fe3O4 Photothermal Nanoprobe. *RSC Adv.* **2017**, *7* (15), 9123–9129. https://doi.org/10.1039/c6ra28413b.

(35) Yang, H.; Zhang, C.; Shi, X.; Hu, H.; Du, X.; Fang, Y.; Ma, Y.; Wu, H.; Yang, S. Water-Soluble Superparamagnetic Manganese Ferrite Nanoparticles for Magnetic Resonance Imaging. *Biomaterials* **2010**, *31* (13), 3667–3673. https://doi.org/10.1016/j.biomaterials.2010.01.055.

(36) Xiong, H.; Zhao, X.; Chen, J. New Polymer - Inorganic Nanocomposites : PEO - ZnO and PEO - ZnO - LiClO 4 Films. **2001**, 10169–10174.

(37) Andhare, D. D.; Patade, S. R.; Kounsalye, J. S.; Jadhav, K. M. Effect of Zn Doping on Structural, Magnetic and Optical Properties of Cobalt Ferrite Nanoparticles Synthesized via. Co-Precipitation Method. *Phys. B Condens. Matter* **2020**, *583* (November 2019), 412051. https://doi.org/10.1016/j.physb.2020.412051.

(38) BEGANSKIENE, A.; SIRUTKAITIS, V.; KURTINAITIENE, M.; JUSKENAS, R.; KAREIVA, A. FTIR, TEM and NMR Investigations of Stöber Silica Nanoparticles. *Mater. Sci.* **2004**, *10* (4), 287–290.

(39) Stefanescu, M.; Stoia, M.; Stefanescu, O. Thermal and FT-IR Study of the Hybrid Ethylene-Glycol-Silica Matrix. *J. Sol-Gel Sci. Technol.* **2007**, *41* (1), 71–78. https://doi.org/10.1007/s10971-006-0118-5.

(40) Xu, P.; Uyama, H.; Whitten, J. E.; Kobayashi, S.; Kaplan, D. L. Peroxidase-Catalyzed in Situ Polymerization of Surface Orientated Caffeic Acid. *J. Am. Chem. Soc.* **2005**, *127* (33), 11745–11753. https://doi.org/10.1021/ja051637r.

(41) Moritz, M.; Geszke-Moritz, M. Amine-Modified SBA-15 and MCF Mesoporous Molecular Sieves as Promising Sorbents for Natural Antioxidant. Modeling of Caffeic Acid Adsorption. *Mater. Sci. Eng. C* **2016**, *61*, 411–421. https://doi.org/10.1016/j.msec.2015.12.093.

(42) Klokkenburg, M.; Hilhorst, J.; Erné, B. H. Surface Analysis of Magnetite Nanoparticles in Cyclohexane Solutions of Oleic Acid and Oleylamine. *Vib. Spectrosc.* **2007**, *43* (1), 243–248. https://doi.org/10.1016/j.vibspec.2006.09.008.

(43) Ştefănescu, M.; Stoia, M.; Ştefănescu, O.; Popa, A.; Simon, M.; Ionescu, C. The Interaction between TEOS and Some Polyols: Thermal Analysis and FTIR. *J. Therm. Anal. Calorim.* **2007**, *88* (1), 19–26. https://doi.org/10.1007/s10973-006-8002-7.

(44) Stoia, M.; Stefanescu, M.; Dippong, T.; Stefanescu, O.; Barvinschi, P. Low Temperature Synthesis of Co2SiO4/SiO2 Nanocomposite Using a Modified Sol-Gel Method. *J. Sol-Gel Sci. Technol.* **2010**, *54* (1), 49–56. https://doi.org/10.1007/s10971-010-2156-2.

(45) Hüsing, N.; Brandhuber, D.; Kaiser, P. Glycol-Modified Organosilanes in the Synthesis of Inorganic-Organic Silsesquioxane and Silica Monoliths. *J. Sol-Gel Sci. Technol.* **2006**, *40* (2–3), 131–139. https://doi.org/10.1007/s10971-006-8802-z.

(46) Brandhuber, D.; Torma, V.; Raab, C.; Peterlik, H.; Kulak, A.; Hüsing, N. Glycol-Modified Silanes in the Synthesis of Mesoscopically Organized Silica Monoliths with Hierarchical Porosity. *Chem. Mater.* **2005**, *17* (16), 4262–4271. https://doi.org/10.1021/cm048483j.

(47) Gittleman, J. I.; Abeles, B.; Bozowski, S. Superparamagnetism and Relaxation Effects in Granular Ni-SiO2 and Ni-Al2O3 Films. *Phys. Rev. B* **1974**, *9* (9), 3891–3897. https://doi.org/10.1103/PhysRevB.9.3891.

(48) Bedanta, S.; Petracic, O.; Kleemann, W. *Supermagnetism*; Elsevier, 2015; Vol. 23. https://doi.org/10.1016/B978-0-444-63528-0.00001-2.

(49) Bruvera, I. J.; Mendoza Zélis, P.; Pilar Calatayud, M.; Goya, G. F.; Sánchez, F. H. Determination of the Blocking Temperature of Magnetic Nanoparticles: The Good, the Bad, and the Ugly. *J. Appl. Phys.* **2015**, *118* (18). https://doi.org/10.1063/1.4935484.

(50) Mamiya, H.; Ohnuma, M.; Nakatani, I.; Furubayashim, T. Extraction of Blocking Temperature Distribution from Zero-Field-Cooled and Field-Cooled Magnetization Curves. *IEEE Trans. Magn.* **2005**, *41* (10), 3394–3396. https://doi.org/10.1109/TMAG.2005.855205.

(51) Dormann, J. L.; Chimie, L. De; Matiere, D.; Pierre, U.; Jussieu, P. *MAGNETIC RELAXATION IN FINE-PARTICLE SYSTEMS*; 1997; Vol. XCVIII.

(52) Muscas, G.; Concas, G.; Cannas, C.; Musinu, A.; Ardu, A.; Orrù, F.; Fiorani, D.; Laureti, S.; Rinaldi, D.; Piccaluga, G.; Peddis, D. Magnetic Properties of Small Magnetite Nanocrystals. *J. Phys. Chem. C* **2013**, *117* (44), 23378–23384. https://doi.org/10.1021/jp407863s.

(53) Hansen, M. F.; Mørup, S. Estimation of Blocking Temperatures from ZFC/FC Curves. *J. Magn. Magn. Mater.* **1999**, *203* (1–3), 214–216. https://doi.org/10.1016/S0304-8853(99)00238-3.

(54) Peddis, D.; Cannas, C.; Musinu, A.; Piccaluga, G. Coexistence of Superparmagnetism and Spin-Glass like Magnetic Ordering Phenomena in a CoFe2O4-SiO2 Nanocomposite. *J. Phys. Chem. C* **2008**, *112* (13), 5141–5147. https://doi.org/10.1021/jp076704d.

(55) Vargas, J. M.; Nunes, W. C.; Socolovsky, L. M.; Knobel, M.; Zanchet, D. Effect of Dipolar Interaction Observed in Iron-Based Nanoparticles. *Phys. Rev. B - Condens. Matter Mater. Phys.* **2005**, *72* (18), 2–7. https://doi.org/10.1103/PhysRevB.72.184428.

(56) Pileni, M. P. Self-Assembly of Inorganic Magnetic Nanocrystals: A New Physics Emerges. *J. Phys. D. Appl. Phys.* **2008**, *41* (13). https://doi.org/10.1088/0022-3727/41/13/134002.

(57) Laureti, S.; Varvaro, G.; Testa, A. M.; Fiorani, D.; Agostinelli, E.; Piccaluga, G.; Musinu, A.; Ardu, A.; Peddis, D. Magnetic Interactions in Silica Coated Nanoporous Assemblies of CoFe 2O4 Nanoparticles with Cubic Magnetic Anisotropy. *Nanotechnology* **2010**, *21* (31). https://doi.org/10.1088/0957-4484/21/31/315701.

(58) Virumbrales, M.; Saez-Puche, R.; Torralvo, M. J.; Blanco-Gutierrez, V. Mesoporous Silica Matrix as a Tool for Minimizing Dipolar Interactions in NiFe2O4 and ZnFe2O4 Nanoparticles. *Nanomaterials* **2017**, *7* (7). https://doi.org/10.3390/nano7070151.

(59) Morup, S.; Bodker, F.; Hendriksen, P. V.; Linderoth, S. Spin-Glass-like Ordering of the Magnetic Moments of Interacting Nanosized Maghemite Particles. *Phys. Rev. B* **1995**, *52* (1), 287–294. https://doi.org/10.1103/PhysRevB.52.287.

(60) Held, G. A.; Grinstein, G.; Doyle, H.; Sun, S.; Murray, C. B. Competing Interactions in Dispersions of Superparamagnetic Nanoparticles. *Phys. Rev. B - Condens. Matter Mater. Phys.* **2001**, *64* (1), 124081–124084. https://doi.org/10.1103/physrevb.64.012408.

(61) Luo, W.; Nagel, S. R.; Rosenbaum, T. F.; Rosensweig, R. E. Dipole Interactions with Random Anisotropy in a Frozen Ferrofluid. *Phys. Rev. Lett.* **1991**, *67* (19), 2721–2724. https://doi.org/10.1103/PhysRevLett.67.2721.

(62) Tartaj, P.; González-Carreño, T.; Serna, C. J. Magnetic Behavior of γ-Fe2O3 Nanocrystals Dispersed in Colloidal Silica Particles. *J. Phys. Chem. B* **2003**, *107* (1), 20–24. https://doi.org/10.1021/jp0260898.

(63) Kechrakos, D.; Trohidou, K. Magnetic Properties of Dipolar Interacting Single-Domain Particles. *Phys. Rev. B - Condens. Matter Mater. Phys.* **1998**, *58* (18), 12169–12177. https://doi.org/10.1103/PhysRevB.58.12169.

(64) Hansen, M. F.; Mørup, S. Models for the Dynamics of Interacting Magnetic Nanoparticles. *J. Magn. Magn. Mater.* **1998**, *184* (3), L262-274. https://doi.org/10.1016/s0304-8853(97)01165-7.

(65) Kelly, P. E.; O'Grady, K.; Mayo, P. L.; Chantrell, R. W. Switching Mechanisms in Cobalt-Phosphorus Thin Films. *IEEE Trans. Magn.* **1989**, *25* (5), 3881–3883. https://doi.org/10.1109/20.42466.

(66) Geshev, J.; Mikhov, M.; Schmidt, J. E. Remanent Magnetization Plots of Fine Particles with Competing Cubic and Uniaxial Anisotropies. *J. Appl. Phys.* **1999**, *85* (10), 7321–7327. https://doi.org/10.1063/1.369356.

(67) García-Otero, J.; Porto, M.; Rivas, J. Henkel Plots of Single-Domain Ferromagnetic Particles. *J. Appl. Phys.* **2000**, *87* (10), 7376–7381. https://doi.org/10.1063/1.372996.

(68) Batlle, X.; García del Muro, M.; Labarta, a. Interaction Effects and Energy Barrier Distribution on the Magnetic Relaxation of Nanocrystalline Hexagonal Ferrites. *Phys. Rev. B* **1997**. https://doi.org/10.1103/PhysRevB.55.6440.

(69) Pfeiffer, H. Determination of Anisotropy Field Distribution in Particle Assemblies Taking into Account Thermal Fluctuations. *Phys. Status Solidi* **1990**, *118* (1), 295–306. https://doi.org/10.1002/pssa.2211180133.

(70) Orrù, F.; Musinu, A.; Cannas, C.; Peddis, D.; Piccaluga, G.; Ardu, A. Interparticle Interactions and Magnetic Anisotropy in Cobalt Ferrite Nanoparticles: Influence of Molecular Coating. *Chem. Mater.* **2012**, *24* (6), 1062–1071. https://doi.org/10.1021/cm203280y.

(71) Peddis, D.; Jönsson, P. E.; Laureti, S.; Varvaro, G. *Magnetic Interactions: A Tool to Modify the Magnetic Properties of Materials Based on Nanoparticles*; 2014; Vol. 6. https://doi.org/https://doi.org/10.1016/B978-0-08-098353-0.00004-X.

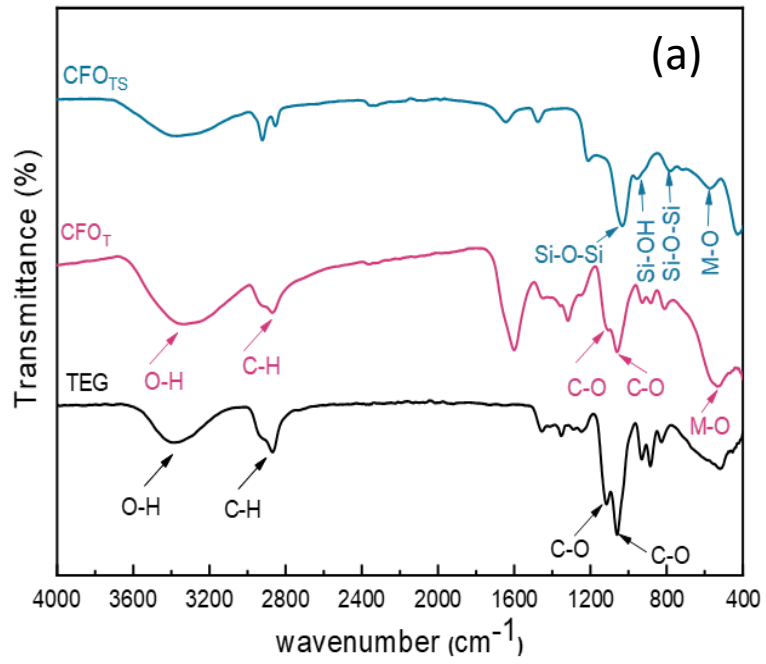

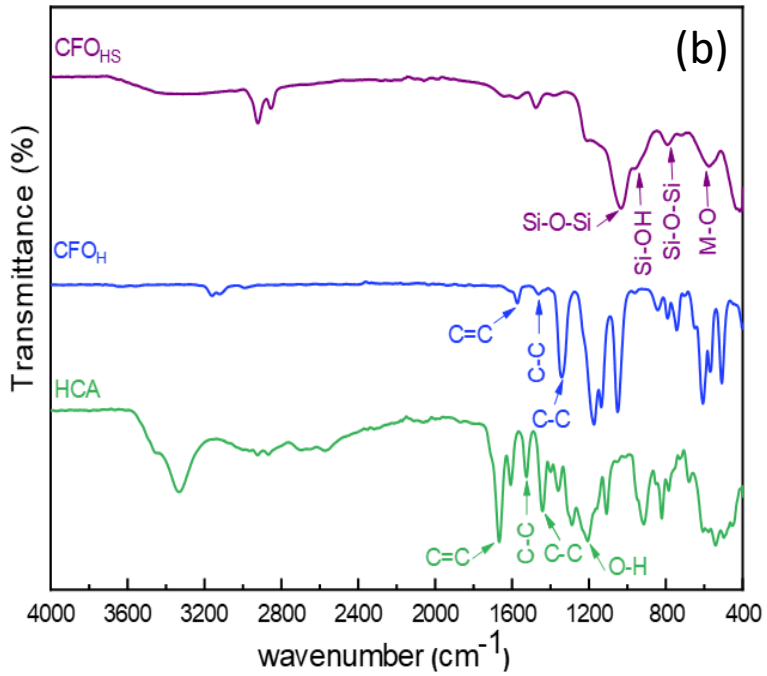

Figure 1: FT-IR for **(a)** TEG, CFO_T CFO_{TS} and **(b)** HCA, CFO_H, CFO_{HS} samples measured in the range 400-4000 cm^{-1}

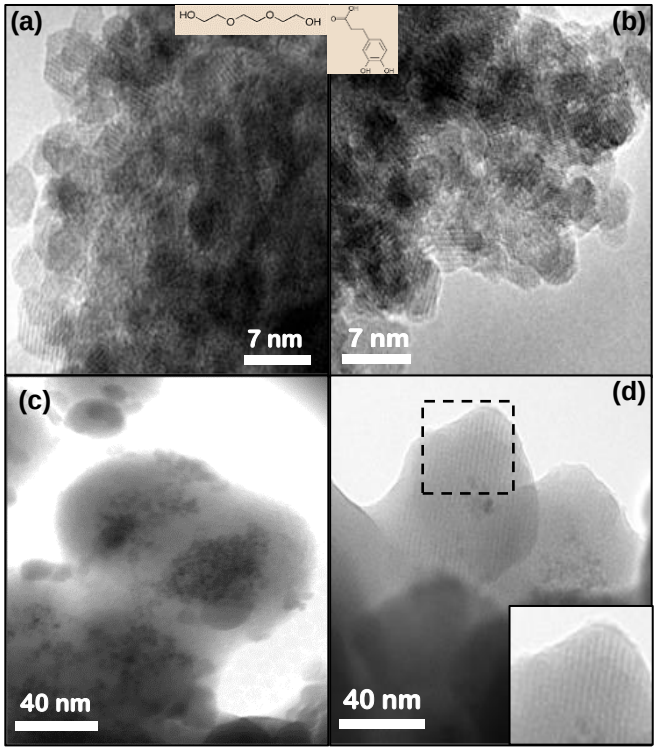

Figure 2: TEM images of **(a)** CFO_T, **(b)** CFO_H, **(c)** CFO_{TS}, and **(d)** CFO_{HS}, samples.

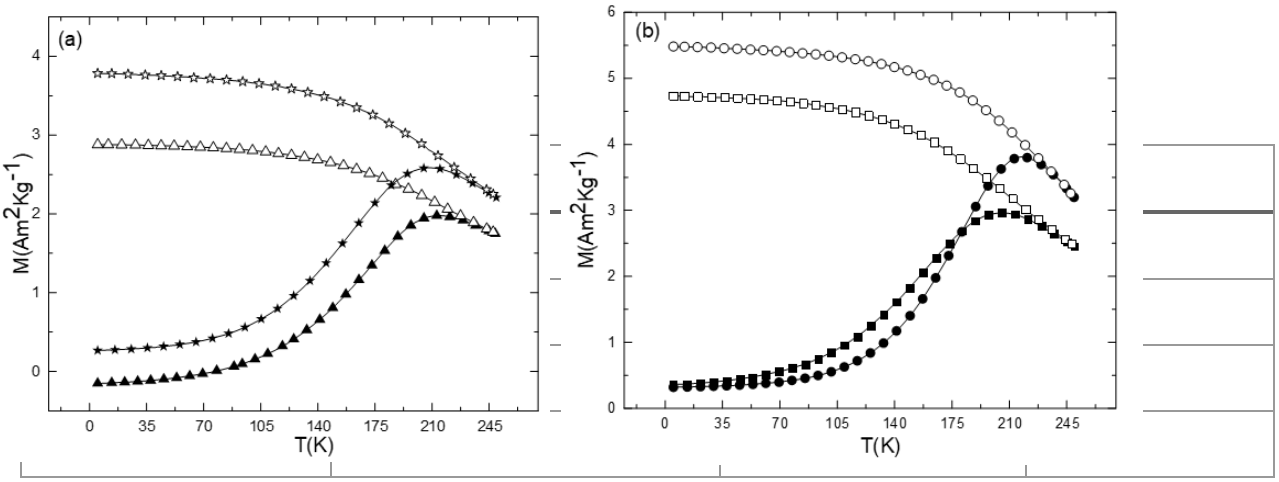

Figure 3. ZFC (full symbols) and FC (empty symbols) curves for the **(a)** CFO_T (triangles) and CFO_{TS} samples (stars), **(b)** CFO_H (circles) and CFO_{HS} (rectangle) samples.

Table1. Temperature Corresponding to the maximum in ZFC Curve (T_{max}), blocking Temperature from ZFC-FC measurements (T_b) and irreversibility temperature (T_{irr}). Uncertainties are given in parentheses.

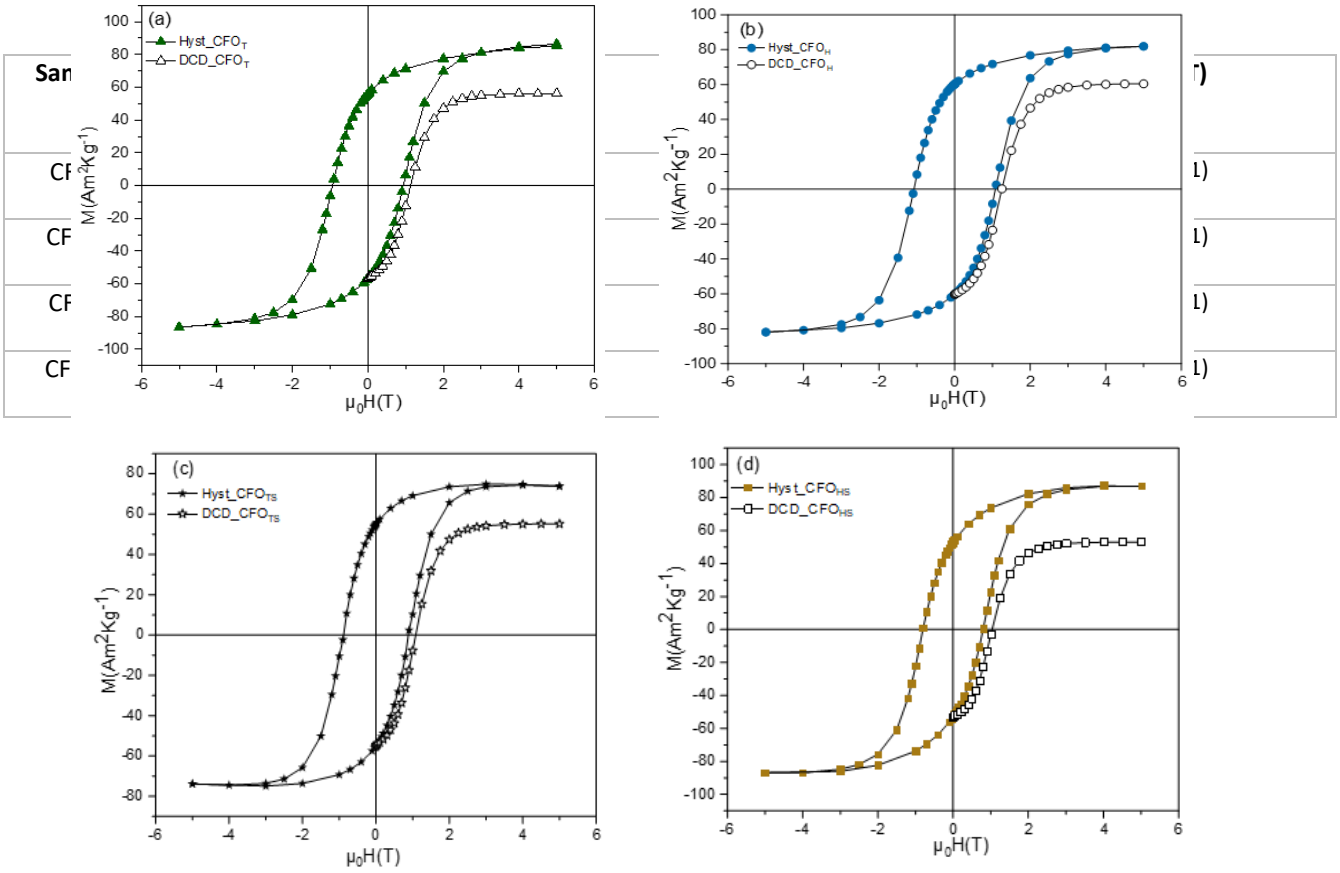

Figure 4: Field-dependence of magnetization and direct current demagnetization (DCD) curves measured at 5 K for **(a)** CFO_T, **(b)** CFO_H samples, and **(C)** CFO_{TS}, (**d)** CFO_{HS} nanocomposites.

Table2: Saturation magnetization (M_s), reduced remanent magnetization (M_r/M_s), saturation filed(μ_0H_k), coercivity (μ_0Hc), remanence coercivity (H_{cr}) at 5 K. Uncertainties are given in parentheses.

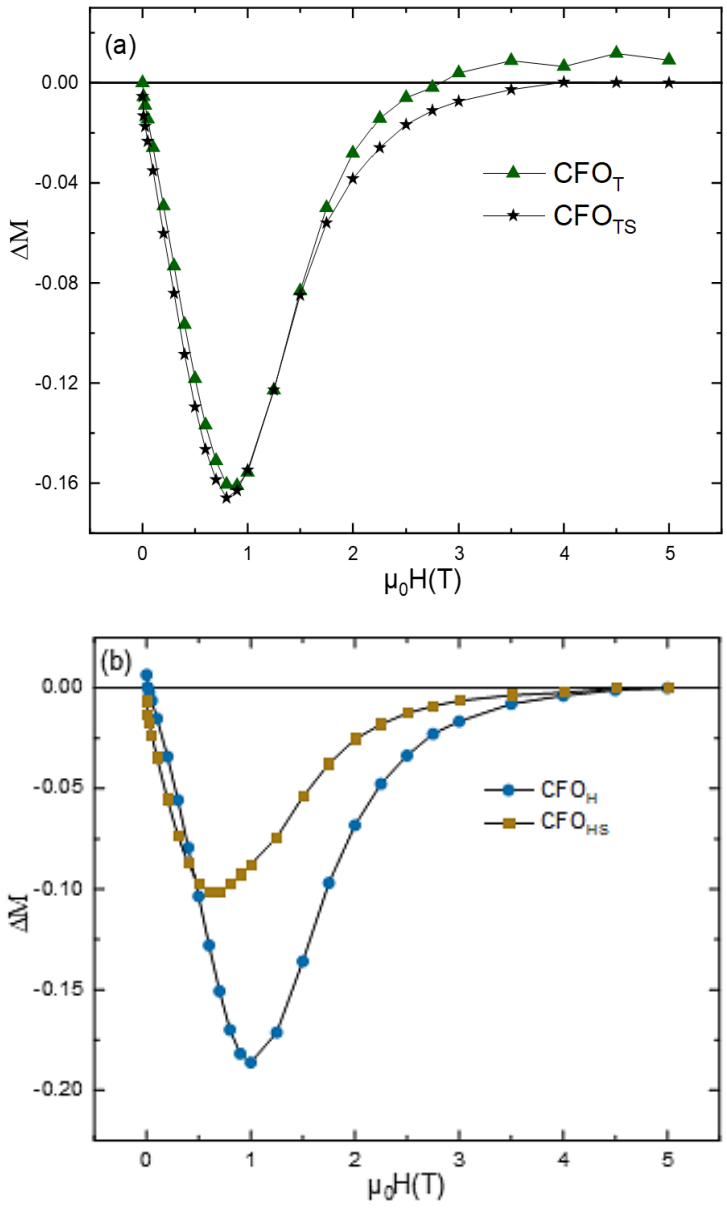

Figure 5: ΔM plots for **(a)** CFO_T, CFO_{TS} and **(b)** CFO_H, CFO_{HS} systems.

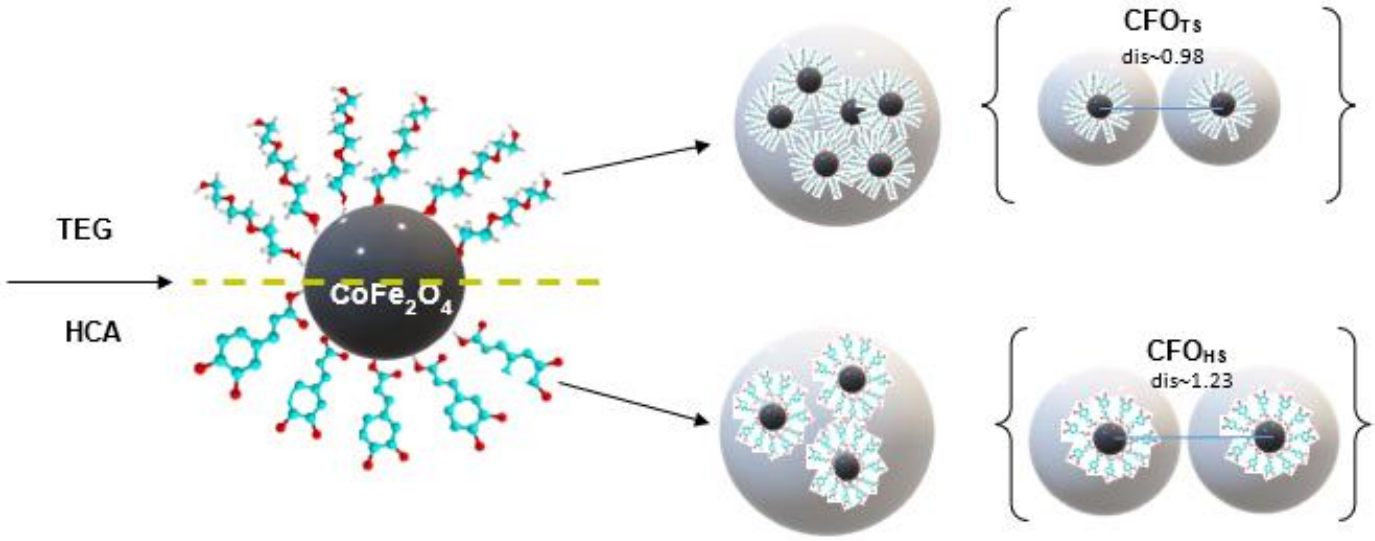

Figure 6: Sketch of the nanoparticles arrangement within a silica structure.